Earth and Planetary Science Letters 533 (2020) 116054

Contents lists available at ScienceDirect

Earth and Planetary Science Letters

www.elsevier.com/locate/epsl

Evolution of subduction dip angles and seismic stress patterns during arc-continent collision: Modeling Mindoro Island

Craig R. Bina [a,*], Hana Čížková [b], Po-Fei Chen [c]

[a] Dept. of Earth and Planetary Sciences, Northwestern University, Evanston, IL, USA
[b] Dept. of Geophysics, Faculty of Mathematics and Physics, Charles University, Prague, Czech Republic
[c] Dept. of Earth Sciences, National Central University, Taoyuan, Taiwan

ARTICLE INFO

Article history:
Received 1 April 2019
Received in revised form 16 August 2019
Accepted 27 December 2019
Available online 15 January 2020
Editor: B. Buffett

Keywords:
subduction dynamics
arc-continent collision
seismic stress fields
mantle transition zone
trench migration
Manila trench

ABSTRACT

Here we dynamically model the temporal development of arc-continent collision, with particular attention to the evolution of slab dip angles and stress fields during approach to collisional locking (suturing). Our modeling is based on a simplified representation of Mindoro Island and the southern Manila Trench, which provide a natural laboratory in that convergence is ongoing to the north but collision is complete in the south, so that distance of 2D slices along the arc may serve as a reasonable proxy for time. We consider in detail the effects of the negative petrological buoyancy imparted to the slab upon encountering the thermally uplifted "410-km" (wadsleyite-forming) phase transition, as well as the effects of initial separation distance between the incoming Palawan continental fragment and the overriding Philippine Mobile Belt assemblage of arc-continent terranes. Despite simplifications in representing this tectonically complex region, our model reproduces important seismic observations, including the progressive steepening of slab dip and the growth of down-dip extensional stresses during the progress of collision. It also reveals that a significant contribution (of order 100 MPa) to the maximum attainable down-dip extensional stress arises from the negative petrological buoyancy of the uplifted "410-km" transition, and it illuminates how the initial separation of arc-continent fragments controls the temporal offset between collisional locking and the onset of negative petrological buoyancy. Finally, associated calculations of maximum shear stress may offer a partial explanation for the aseismic nature of tomographically proposed slab extensions below the Wadati-Benioff zone.

1. Introduction

Dynamical models of oceanic subduction exhibit patterns of temporal evolution in convergence rates, slab dip angles, and stress fields, among other properties (Čížková and Bina, 2013, 2015, 2019). Introduction of arc or continental collision into such models should lead to eventual cessation of convergence (Magni et al., 2012), with concomitant effects on dip angles and stress fields. Mindoro Island and the southern Manila Trench (northward toward Luzon) provide a natural laboratory for studying such evolution of arc-continent collisions. Distance along the arc may serve as an effective proxy for time, with convergence ongoing to the north but collision essentially complete (in the sense of vanishing convergence rates and seismic slip) to the south. Here we analyze simple 2D geodynamical models of such an arc-continent collision, in an effort to better understand the associated evolution of slab dip angles and stress fields, along with the forces driving such evolution, and we compare the model results to regional seismological observations.

The Manila Trench is a predominantly N-S trending, east-dipping trench, extending from offshore SW Taiwan in the north to offshore NW Mindoro in the south. Both ends of the Manila Trench are terminated by arc-continent collisions. To the north, the Luzon Arc (LA) began to rapidly collide with the Chinese Continental Margin (CCM) in Mio-Pliocene times (ca. 5 Ma) (Teng, 1990). To the south, the Palawan Continental Block (PCB: a continental fragment) indented into the Philippine Mobile Belt (PMB: an accretion of arc terranes and continental fragments) during the Miocene (Yumul et al., 2003). Plate kinematic models suggest that current convergence rates fall from greater than 7 cm/yr in the north (~19°N) of the arc to less than 2 cm/yr in the south (~13°N) of the arc near Mindoro (Hamburger et al., 2010).

Here we first compare bathymetries and slab geometries of S Taiwan and offshore with those of NW Mindoro and offshore (Fig. 1). Then, we focus on the southern end of the Manila Trench, along which Oligocene seafloor of the Sundaland plate subducts

* Corresponding author.
E-mail address: craig@earth.northwestern.edu (C.R. Bina).

https://doi.org/10.1016/j.epsl.2019.116054
0012-821X/

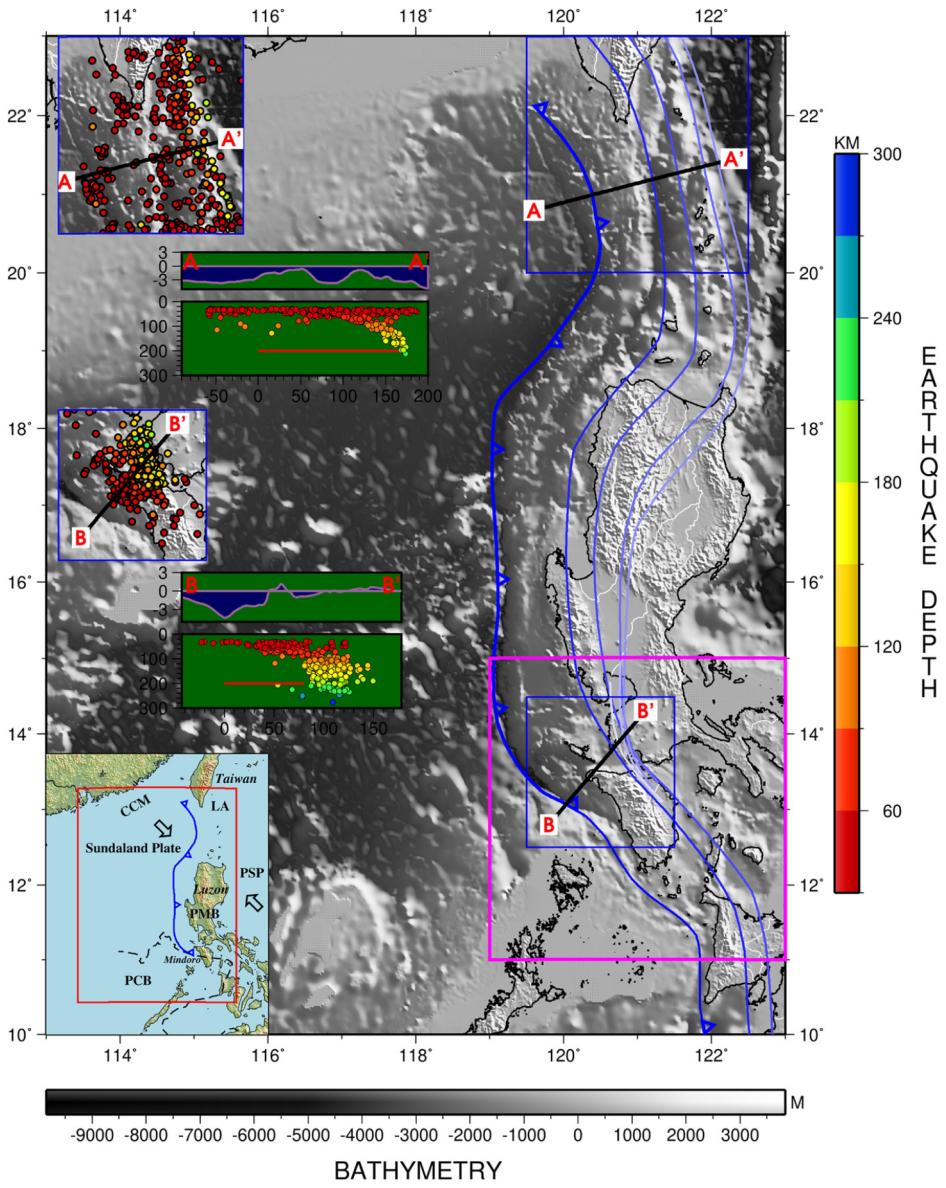

Fig. 1. Bathymetry of the Manila trench (dark blue toothed curve), with contours of slab depth (light blue curves). Central green insets show bathymetry (upper panels) and slab geometry (from earthquake hypocenters >30 km depth) along trench-normal cross-sections for the S Taiwan region (A-A′) and the NW Mindoro region (B-B′), where red bars indicate slab-trench distances (measured at 200 km depth). Steeper dip angles are seen for the older collision in Mindoro, relative to the younger collision in Taiwan. Left gray insets show epicenters in map view along these same two profiles, corresponding to blue boxes on main bathymetric map. Lower left pale blue inset shows broader map of overall tectonic scenario: CCM = Chinese Continental Margin, LA = Luzon Arc, PSP = Philippine Sea Plate, PMB = Philippine Mobile Belt, PCB = Palawan Continental Block (outlined by dashed line), arrows indicate directions of plate motion. Pink box on main bathymetric map outlines area shown later in Fig. 2. (For interpretation of the colors in the figure(s), the reader is referred to the web version of this article.)

eastward beneath the PMB at the western edge of the Philippine Sea plate (PSP), the southern terminus of which occurs at Mindoro Island, marking the locus of Miocene collision between the PCB from the west and the PMB from the east (Fig. 1). With the southern Manila Trench exhibiting ongoing convergence to the north (at SW Luzon), decreasing convergence southward (to offshore NW Mindoro), and cessation of convergence due to complete collision in the south (at onshore SW Mindoro), we adopt NNW-SSE distance along the arc as a potential model proxy for time-progression of collision (Chen et al., 2015).

We construct a simple 2D geodynamic model of subduction in which the overriding plate contains a continental block ∼500 km in width, representing the PMB. The subducting plate consists initially of oceanic lithosphere ∼400 km wide with a mid-Oligocene age of ∼26 Ma at the trench, followed by a continental block ∼400 km in width to represent the PCB. The initial convergence rate is ∼2 cm/yr, as described in the further model details given below. As the model arc-continent collision progresses, we track the evolution of slab dip angles and principal stress patterns, for comparison with local seismotectonic observations, over 50-Myr model runs with particular focus on the first ∼17 Myr. In order to isolate collisional effects, models exhibiting collision are compared to equivalent models without collision simply by shifting the incoming PCB continental block much further outboard, so that collision does not occur within the time frame of the model. Buoyancy effects arising from thermal deflection of equilibrium mantle phase transitions are isolated by the simple expedient of setting their Clapeyron slopes to zero, for comparison to equivalent models with normal Clapeyron slopes. We also vary the initial separation of continental fragments and the depth-extent of the arc-like continental fragment on the overriding plate.

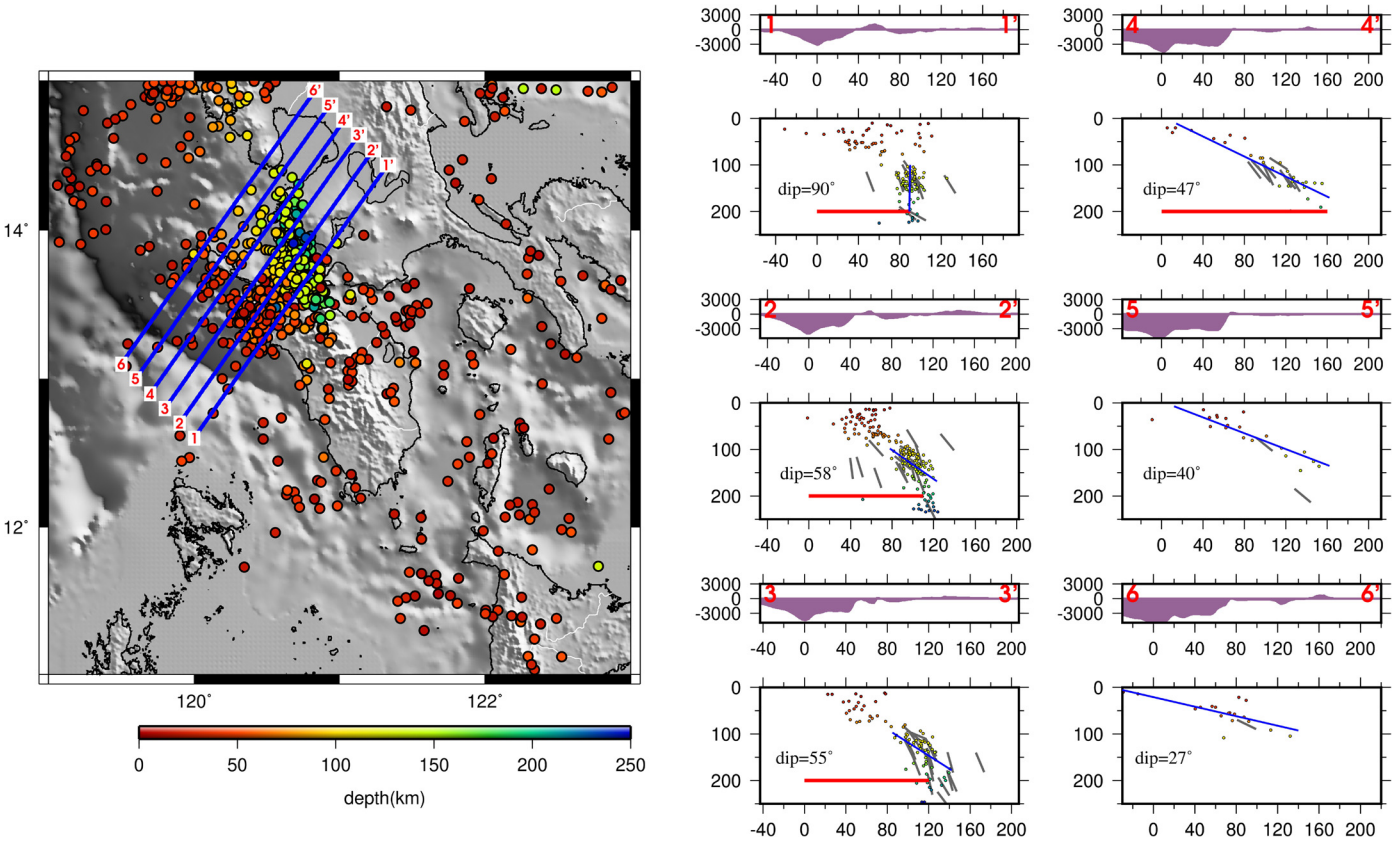

Fig. 2. Distribution of earthquakes in Mindoro-Luzon region (left). Hypocenters (from EHB catalog) clustered in NW Mindoro and SW Luzon are projected onto six cross-sections, showing bathymetry (upper panels) and variations in Wadati-Benioff dip angles from SE to NW along trench (right side). Dip angles are determined by linear fitting of seismicity (blue lines); for regions of bending slabs (profiles 1-3), the 100-200 km depth range was used for fitting. Red bars indicate slab-trench distances (measured at 200 km depth). Gray line segments show plunges of **T**-axes of intermediate-depth subduction earthquakes (from GCMT catalog) projected on the cross-sections – showing predominantly down-dip extensional stresses. Figure modified from Figs. 4 and 7 of Chen et al. (2015).

Our goal is primarily to study the evolution of slab dip angles and slab stress fields during the progress of subduction and onset of collision. While we cannot hope to reproduce in detail the evolution of such a complex region using a simple 2D model, we aim to better understand the overall trends in evolution of dip and stress. We also seek to understand the role of petrological buoyancy forces associated with mantle phase transitions in governing such trends.

There are few previous 2D dynamical modeling studies focused on the evolution of slab dip and stresses during continental collisions. The best comparison case may be that of Magni et al. (2012), to which we will refer repeatedly, whose study used a model setup similar to our own, but it did not explicitly track dip angles or stress fields through convergence and collision, although it did observe rotation of the slab to a vertical position after collisional locking. In addition there are the studies of Ghazian and Buiter (2013) and François et al. (2014). Both of these latter studies employ thermomechanical models of continental collisions with prescribed (kinematic) convergence rates, and both report increases in dip angle (the former gradual increase beyond 40° and the latter increases from 45° to ∼80°), but neither features mantle phase transitions. Finally, the studies of Duretz et al. (2011) and Baumann et al. (2010) employ thermomechanical models of continental collisions with kinematic initial runs followed by fully dynamical development, and both include mantle phase transitions, but both focus almost exclusively on the phenomena of slab detachment during advanced stages of collision, beyond the time frame of our primary focus here.

2. Seismological observations

Although our geodynamic modeling focuses primarily on using distance along the arc as a proxy for temporal progression of arc-continent collision in the region of Mindoro Island and the southern Manila Trench (northward toward Luzon), in the framework of the seismological observations outlined below, additional insight into such temporal progression can be gained by examination of the northern end of the Manila Trench near Taiwan. Taiwan and Mindoro both formed by arc-continent collision and bear such similarities as frequent earthquakes and high mountain ranges, but the fact that their respective collisions occurred at different times – the Mio-Pliocene for Taiwan (Teng, 1990) versus the Miocene for Mindoro (Yumul et al., 2003) – provides another opportunity to envision the time evolution of arc-continent collisional processes.

Fig. 1 shows a comparison of bathymetries and slab geometries of S Taiwan and offshore with those of NW Mindoro and offshore. Two rectangular boxes, based on seismic distributions in regions of offshore S Taiwan and offshore NW Mindoro, were selected to project earthquakes with depths greater than 30 km and associated bathymetry. Earthquakes were drawn from the EHB catalogue (Engdahl et al., 1998), and the projection profile was determined by minimum misfits of linear fitting on projecting earthquakes with depths greater than 80 km (Chen et al., 2001). The profiles thus derived are roughly perpendicular to the trench upon a posteriori examination. Bathymetries were also projected onto the profiles to investigate and compare their relationships with subducting slabs. Generally steeper dip angles are evident for the more advanced stage of collision in Mindoro, relative to the younger collisional event in Taiwan.

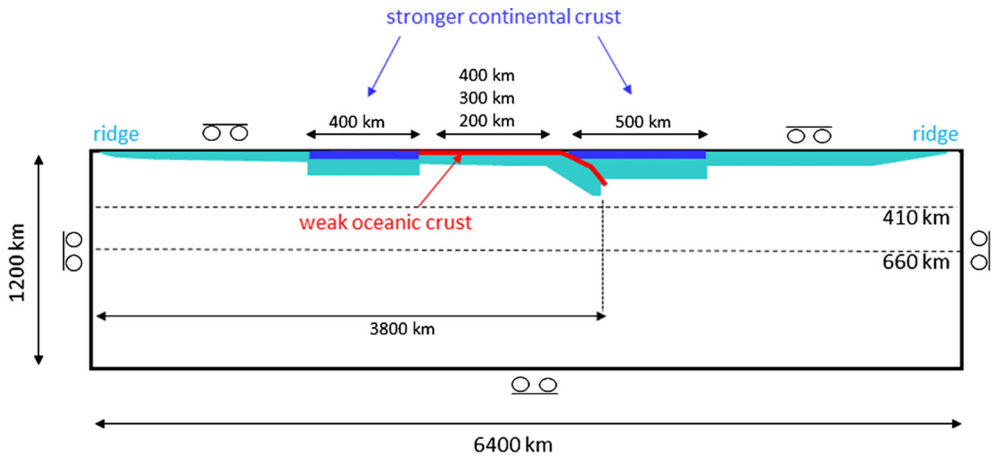

Fig. 3. Setup of the dynamical model. Subducting and overriding plates are decoupled by weak oceanic crust (red). Dark blue indicates continental fragments. Dashed lines mark the major phase transitions at 410 km and 660 km depths. Details given in text.

Recent seismic observations in the Mindoro-Luzon region are summarized in Fig. 2. Hypocentral distributions from the EHB catalog indicate that the dip angle of the Wadati-Benioff zone increases from NW to SE along the arc, with steepening occurring first by flexure of the slab near ∼150 km depth followed by propagation of the steepening to shallower depths (Chen et al., 2015). Thus, dip angles as determined by seismicity are observed to increase from regions of ongoing convergence (offshore SW Luzon) to regions of cessation of convergence (NW Mindoro thrust belt). Best-fit dip angles to hypocentral distributions are observed to increase from ∼30° in the NW to ∼90° in the SE at Mindoro. Slab-trench distance (measured at 200 km depth) decreases as dip angle increases.

Orientations of **P**- and **T**-axes for intermediate-depth (∼80-300 km) earthquake focal mechanisms indicate that down-dip tension dominates the stress patterns within the slab, suggesting a causal relationship with negative slab buoyancy (Chen et al., 2015). Also in Fig. 2, earthquakes from the GCMT catalog (Ekström et al., 2012) are shown with their **T**-axes projected onto the planes of cross-section (as their steep plunges and down-dip orientations render them relatively insensitive to trench-normal cross-sectional azimuths), illustrating this pattern of predominantly down-dip extensional stresses. In general, within each cross-section, the extensional stress axes are observed to dip slightly more steeply than the best-fit dip angles to hypocentral distributions (suggesting that stress orientation may serve as a temporally leading indicator of increasing dip), the exception being in section 1-1' where the best-fit slab dip is vertical.

While recorded seismicity extends only to ∼250 km depth, seismic tomography suggests deeper aseismic extension of the slab to ∼400 km depth. This is true to the north beneath Taiwan (Chen et al., 2004b), but it is also true in both the southern and northern regions of the Manila Trench and in the region of Mindoro Island itself (Fan et al., 2015, 2016, 2017) in particular. Tomographic resolution, however, is insufficient to determine whether there is significant variation in maximum depth of aseismic extension along the arc (Fan et al., 2017), although there is some (as yet not statistically significant) hint of deeper extension to the south in recent unpublished data (Chen et al., 2018).

3. Geodynamic model

To model subduction dynamics we solve the governing equations in the extended Boussinesq approximation without internal heating (Čížková et al., 2007) using a finite-element method in the SEPRAN package (Segal and Praagman, 2005). A portion of the mantle 6400 km wide by 1200 km deep is represented as a 2D Cartesian model domain (Fig. 3) with impermeable free-slip boundaries. The subducting plate extends from a ridge in the top left corner of the model to the trench initially located 3800 km from the ridge. Another ridge located in the top right corner of the model ensures horizontal mobility of the overriding plate (Čížková and Bina, 2013).

Initial temperature distributions in subducting and overriding plates follow a cooling half-space model for lithosphere of a given age, where the age of the plate at the trench, having formed in the mid-Oligocene, is 25 Myr, and in which thermal diffusivity is assumed constant (10^{-6} m^2/s). An adiabatic temperature profile is prescribed below the plates, with a potential temperature of 1573 K, where assumed thermal expansivity decreases with depth from 3×10^{-5} K^{-1} at the surface to 1×10^{-5} K^{-1} at 2800 km depth (Chopelas and Boehler, 1992; Hansen and Yuen, 1994; Katsura et al., 2009).

The subducting plate tip is prescribed to extend to a depth of 80 km along an arc with radius of 200 km. In order to facilitate the onset of subduction, we then first develop a slab tip by executing a preliminary kinematic run with a fixed velocity of 2 cm/yr prescribed at the top of the subducting plate. The tip is thus driven to a depth of 200 km. Then the driving velocity is switched off and a free-slip condition is prescribed on all boundaries. The end of this kinematic initialization represents the initial moment $t = 0$ of all dynamical model calculations, since from that moment onward slab buoyancy is the only driving force in the system. This initial depth of 200 km is chosen to be as small as possible while allowing for dynamical subduction to proceed after the kinematic initialization. (For comparison, Magni et al. (2012) start with a slab extending to 300 km depth.) The initial velocity of 2 cm/yr is chosen because the subducting seafloor is mid-Oligocene in age, while collision occurred in the mid-Miocene (Sarewitz and Karig, 1986; Zahirovic et al., 2014). A minimum mean convergence rate of ∼2 cm/yr is required for 25 Ma lithosphere to subduct to a depth of ∼300 km in the ∼15 Myr between the mid-Oligocene and the mid-Miocene, so we used 2 cm/yr as the initial kinematic rate, but thereafter it is controlled by the dynamics of the model.

Major mantle phase transitions at depths of 410 km and 660 km are incorporated (both buoyancy and latent heat effects) using a phase function with harmonic (sinusoidal) parameterization (Čížková et al., 2007). The Clapeyron slope of the exothermic "410-km" olivine-wadsleyite transition is set at 2 MPa/K, and that of the endothermic "660-km" bridgmanite-forming transition is set at −2.5 MPa/K. These were adopted from the ranges given by Bina and Helffrich (1994), as described in Čížková and Bina (2015), but, as described in Čížková and Bina (2019), the value for the olivine-wadsleyite transition was reduced to account for the ob-

Table 1
Symbols and model parameters.

Symbol	Meaning	Value	Units
Upper mantle and transition zone rheology			
A_{diff}	Pre-exponential parameter of diffusion creep[a]	1×10^{-9}	$Pa^{-1}\,s^{-1}$
A_{disl}	Pre-exponential parameter of dislocation creep[a]	3.1×10^{-17}	$Pa^{-n}\,s^{-1}$
E_{diff}	Activation energy of diffusion creep[a]	3.35×10^{5}	$J\,mol^{-1}$
E_{disl}	Activation energy of dislocation creep[a]	4.8×10^{5}	$J\,mol^{-1}$
V_{diff}	Activation volume of diffusion creep[a]	4.8×10^{-6}	$m^3\ mol^{-1}$
V_{disl}	Activation volume of dislocation creep[a]	11×10^{-6}	$m^3\ mol^{-1}$
N	Power-law exponent	3.5	–
η_{crust}	Viscosity of crust	10^{20}	Pa s
τ_y	Yield stress	5×10^{8}	Pa
e_y	Reference strainrate	10^{-15}	s^{-1}
n_y	Stress limiter exponent	10	–
P	Hydrostatic pressure	–	Pa
R	Gas constant	8.314	$J\,K^{-1}\ mol^{-1}$
T	Temperature	–	K
e	Second invariant of the strainrate	–	s^{-1}
Lower mantle rheology			
A_{diff}	Pre-exponential parameter of diffusion creep	1.3×10^{-16}	$Pa^{-1}\,s^{-1}$
E_{diff}	Activation energy of diffusion creep[b]	2×10^{5}	$J\,mol^{-1}$
V_{diff}	Activation volume of diffusion creep[b]	1.1×10^{-6}	$m^3\ mol^{-1}$
Other model parameters			
κ	Diffusivity	10^{-6}	$m^2\ s^{-1}$
G	Gravitational acceleration	9.8	$m\,s^{-2}$
ρ_0	Reference density	3416	$kg\,m^{-3}$
c_p	Specific heat	1250	$J\,kg^{-1}\ K^{-1}$
α_0	Surface thermal expansivity	3×10^{-5}	K^{-1}
$\Delta\alpha$	Expansivity contrast	0.415	–
γ_{410}	Clapeyron slope 410 km phase transition[c]	$0, 2 \times 10^{6}$	$Pa\,K^{-1}$
γ_{660}	Clapeyron slope 660 km phase transition[c]	-2.5×10^{6}	$Pa\,K^{-1}$
$\delta\rho_{410}$	Density contrast 410 km phase transition[d]	273	$kg\,m^{-3}$
$\delta\rho_{660}$	Density contrast 660 km phase transition[d]	341	$kg\,m^{-3}$

[a] Parameters of wet olivine based on Hirth and Kohlstedt (2003).
[b] Čížková et al. (2012).
[c] Bina and Helffrich (1994), Čížková and Bina (2015, 2019).
[d] Steinbach and Yuen (1995).

servation by Arredondo and Billen (2016) that use of pure-olivine Clapeyron slopes exaggerates phase transition dynamical effects in a pyrolitic mantle. We also execute models in which the 410-km phase-transition Clapeyron slope is set to zero, for reference. As in our previous studies, we limit our focus here to equilibrium phase transitions. While there is a vibrant literature on potential effects of metastable olivine and pyroxene, that falls beyond the scope of this study. Moreover, the warm thermal regime of slow subduction of young lithosphere in this region is unlikely to allow for metastability.

Upper-mantle rheology follows a composite model (van den Berg et al., 1993) combining diffusion creep, dislocation creep, and a power-law stress limiter (approximating Peierls creep) (van Hunen et al., 2002), with activation parameters based on wet olivine rheology (Hirth and Kohlstedt, 2003). Lower-mantle rheology is based on diffusion creep with activation parameters derived from slab sinking-speed analysis (Čížková et al., 2012). (Sinking-speed analysis involves constraining deep mantle viscosity by correlation of geodynamic models with empirical estimates of slab sinking speeds as derived from tectonic reconstructions over the past 300 Myr based on seismic tomography of subducted lithosphere in the lower mantle.) Details of the rheological model are given in the Appendix, and parameters are specified in Table 1.

A weak, 10-km thick, oceanic crust-like layer is placed on the surface of the subducting plate (Běhounková and Čížková, 2008), the low viscosity (10^{20} Pa s) of which controls decoupling between the subducting and overriding plates. Below 200 km depth, it is replaced by mantle material. No intrinsic density contrast is assigned to this oceanic crustal layer. From a modeling perspective, the collision is referred to as "complete" when all of this weak oceanic crustal layer has been consumed by subduction, essentially locking the continental collision, but deformation may continue well beyond this point.

A piece of strong (5×10^{22} Pa s) continental crust (representing the PMB), ∼500 km wide, is placed at the leading edge of the overriding plate. A second piece of strong continental crust (representing the PCB), ∼400 km wide, is placed on the subducting plate. Initial separation between the two continental fragments, which ultimately constrains the length of the slab, is 400 km (although we also examine cases of 200-km and 300-km separation for comparison). Both pieces of continental crust are assumed to be buoyant (density contrast with respect to underlying mantle lithosphere is 600 kg/m^3, the same as in Magni et al. (2012)) and thick (a standard 35 km), and they are underlain by 100-km-thick cold lithosphere. Here cold lithosphere is represented by a cooling half-space model with an age of 130 Myr, in which sub-continental viscosity falls to the level of the mean upper mantle viscosity by a depth of ∼135 km. (Note the subtle difference from the model of Magni et al. (2012), in which 40 km of crust overlies ∼150 km of lithosphere, the latter with a linear temperature gradient.) We also examined a model in which the continental fragment on the subducting plate is absent, for reference, as well as a model in which the continental fragment on the overriding plate is underlain by thinner (∼50 km) cold lithosphere.

We study the dynamical evolution of subduction over 50-Myr model runs, focusing particularly on the stress evolution during the first ∼17 Myr. Our primary tests focus on the effects of varying phase transition Clapeyron slopes and initial separation (prior to the preliminary kinematic run) of continental fragments. Our secondary tests involve switching the presence or absence of the continental fragment on the subducting plate and varying the depth-

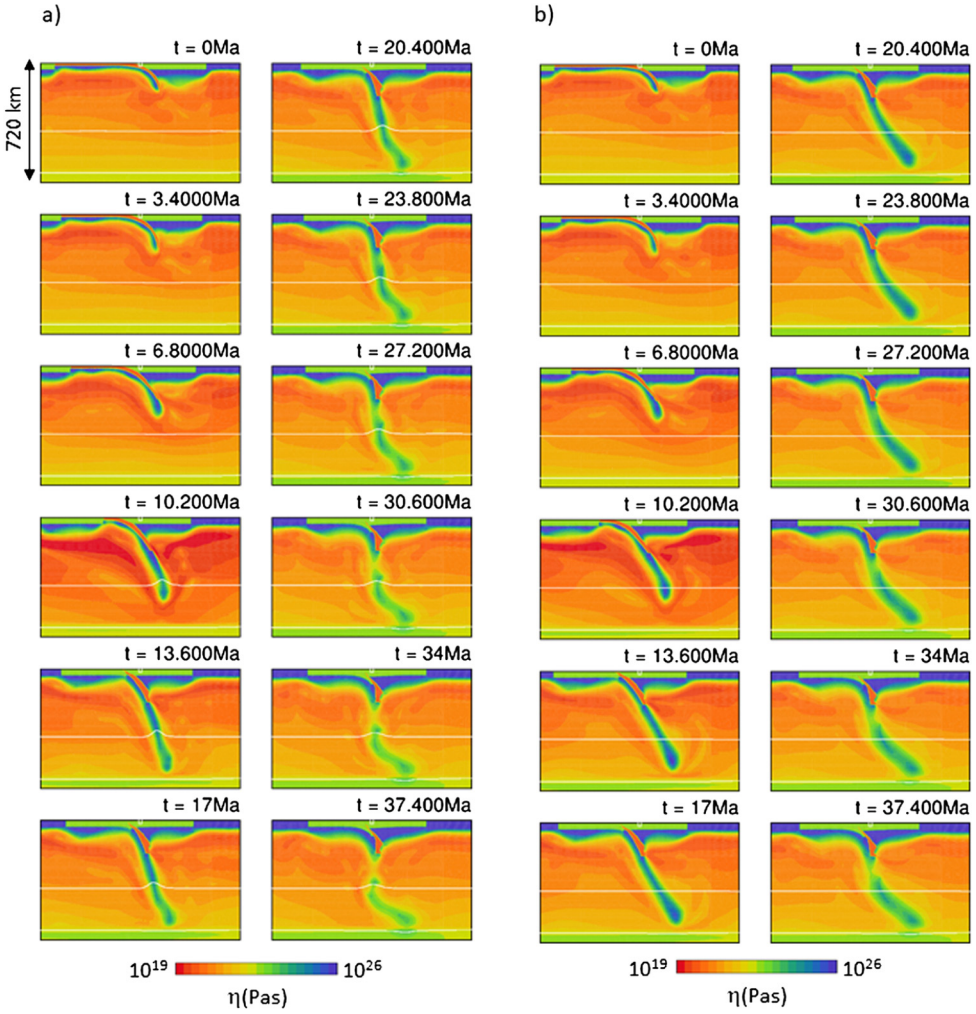

Fig. 4. Viscosity snapshots (1:1) illustrating evolution of dynamical model of subduction, including arc-continent collision followed by locking (suturing) and slab detachment. Left (a): case of normal 410-km Clapeyron slope. Right (b): case of zero 410-km Clapeyron slope. Small white square denotes original location of trench. Continental fragment reaching trench is slowly dragged into subduction channel, where its higher viscosity and lower density lead to continuous reduction of convergence velocity until subduction virtually stops.

extent of the arc-like continental fragment at the leading edge of the overriding plate. We particularly analyze the evolution of the slab dip angle and of both the magnitudes and orientations of the principal deviatoric stresses arising in the slab. Dip angle is evaluated in the depth range 100-200 km using a chain of monitor tracers placed at the bottom of the oceanic crust.

4. Results

4.1. Evolution of slab dip angles

Evolution of the dynamical model of subduction is illustrated in a series of snapshots in Fig. 4. When the continental fragment on the subducting plate reaches the trench and collides with the crustal fragment on the overriding plate, it is slowly dragged into the subduction channel. Due to its higher viscosity compared to the oceanic crust that was entering the subduction channel before, the lubricating effect is significantly reduced and the viscous coupling between the subducting and overriding plates is strengthened. Together with the reduction of the subducting plate's negative buoyancy due to the buoyant continental crustal fragment, this leads to continuous reduction of the convergence velocity from ∼1 cm/yr at 15 Myr to values of ∼0.1 cm/yr at 30-40 Myr and subduction virtually stops.

Significant slab rollback, which acts to reduce dip angle (Čížková and Bina, 2013), is not possible beyond ∼8 Myr, due to the proximity to the trench of the incoming, intrinsically buoyant, continental fragment on the subducting plate. Thereafter, in this state of incipient collision, trench retreat is succeeded by trench advance (in agreement with Magni et al. (2012) and with models of arc collisions with low-density oceanic plateaux (Mason et al., 2010)), and slab dip begins to increase due to the combined effects of the negative thermal buoyancy of the cold slab and the negative petrological buoyancy arising from upward deflection of the Clapeyron-positive equilibrium wadsleyite-forming "410-km" phase transition (accompanied by rheological weakening at the slab hinge). Slab dip continues to increase even after subduction locking (suturing) upon full arc-continent collision, due to these same buoyancy forces which eventually induce further slab weakening, necking, and detachment (Baumann et al., 2010; Duretz et al., 2011; Magni et al., 2012). Model dip angles (Fig. 5) increase over time from ∼45° to ∼90°, just as they are seen to do in the seismic data (Fig. 2).

4.2. Effects on dip angles of phase transitions and initial continental separation distance

Comparison of this reference case (Fig. 4a) to model runs in which the Clapeyron slope of the 410-km phase transition is set

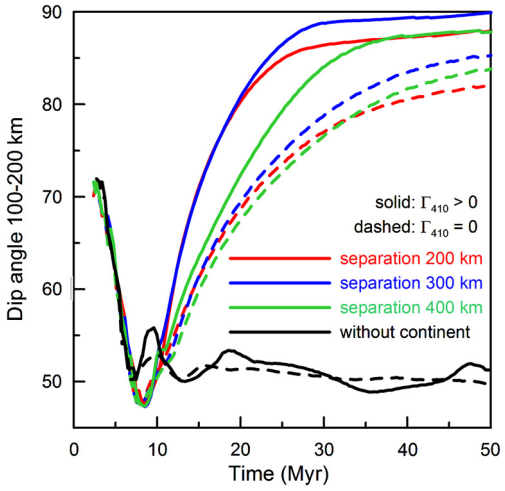

Fig. 5. Evolution of slab dip angle for reference case of 100-km deep continental fragments. Solid lines denote normal 410-km Clapeyron slope, and dashed lines denote zero Clapeyron slope (i.e., no petrological buoyancy). Colors denote varying initial continental separation distances, with black denoting effectively infinite separation (i.e., no continental fragment on subducting plate). Note that effect of 410-km phase transition is to enhance increase in dip angle.

to zero (thereby preventing equilibrium thermal deflection and eliminating any associated petrological buoyancy) reveals that the effects of the phase transition include larger dip angles, shallower depths of slab necking, and earlier (by ∼7 Myr) slab detachment (Fig. 4b). The primary effect of the phase transition, to enhance the temporal increase in slab dip angle, is quantified in Fig. 5.

Also shown in Fig. 5 is the effect of varying the initial continental separation (effectively varying the temporal separation between the onset of negative petrological buoyancy and subduction locking by varying the length of the slab), with the result that smaller initial separation yields not only earlier collision but also somewhat more rapid steepening of dip angles (followed by earlier detachment). For example, at ∼20 Myr, the dip angle is steeper due to phase transition by ∼5° in the case of 400-km separation but by ∼13° in the case of 300-km separation, for reasons discussed below. Not shown is the effect of decreasing the depth-extent of the arc-like continental fragment at the leading edge of the overriding plate, which is found to yield only slightly faster subduction, with a maximum dip angle ∼5° larger than the reference case being attained ∼5 Myr earlier. Finally, the effect of removing the colliding continental fragment from the subducting plate is to eliminate subduction locking, rapid dip increase, and slab detachment, while the presence of phase transitions in this case acts to induce some small oscillations in dip angle attendant upon slab buckling and stagnation (Čížková and Bina, 2013).

4.3. Evolution of slab stress fields

In addition to slab dip angles, our dynamical models yield evolving stress patterns within slabs, which can be compared to those elucidated from earthquake focal mechanisms (Ito and Sato, 1992; Bina, 1997; Chen et al., 2001, 2004a; Čížková et al., 2007; Čížková and Bina, 2015; Zahradník et al., 2017). Model evolution of principal deviatoric stresses is illustrated in Fig. 6. The dominant pattern of down-dip extensional stresses, arising from negative buoyancy of the slab, is clearly visible. The two panels show stress fields at 10.20 Myr and 10.88 Myr, just before and just after (respectively) the slab begins to experience the effect of the (thermally uplifted) 410-km discontinuity during the progress of collision. The collisional process is occurring but is not yet complete, and our goal is to examine the evolution of dip and stress during the collisional process (during the approach to complete collision), so that this figure illustrates the combined effects of the 410-km phase transition and ongoing collision. As the effect of negative petrological buoyancy arising from thermal uplift of the 410-km phase transition takes hold, supplementing the ongoing negative thermal buoyancy, both the dip angles and magnitudes of intermediate-depth tensional stresses can be seen to increase.

4.4. Effects on stress fields of phase transitions

Fig. 7 shows the temporal evolution of the magnitude of the maximum deviatoric principal extensional stress at a sampling depth of 250 km in the slab, both for the reference case and for the case in which the 410-km Clapeyron slope is set to zero (thereby preventing equilibrium thermal deflection and eliminating the associated petrological buoyancy). Here the temporal increase in magnitude of extensional stresses can be seen to generally track the increase in slab dip angle. Moreover, the contribution of the petrological buoyancy force arising from thermal deflection of the equilibrium wadsleyite-forming transition can be seen to amount to ∼100 MPa of additional extensional stress. Similar results are obtained at sampling depths of 150, 200, 300, and 350 km.

4.5. Effects on stress fields of initial continental separation distance

Also evident in Fig. 7 is an effect of varying initial separation of continental fragments, as at 400-km separation the slab tip encounters the uplifted “410-km” phase transition slightly before subduction locking, whereas at 300-km separation these two events are roughly contemporaneous. For the cases with a 410-km Clapeyron slope of zero (dashed), the amplitude of the local maximum increases with increasing initial separation distance. This is because the tension arises solely from the negative thermal buoyancy of the slab, and there is a greater length of slab hanging in the mantle (prior to collisional locking) for larger initial separation distances. The exception is the no-continent case (essentially an infinite initial separation distance), in which the absence of collisional locking (as there is no intrinsically buoyant and highly viscous continent at the surface) damps the maximum attainable extensional stress.

In the no-continent case of essentially infinite initial separation (black), the slab sinks much faster, due to the absence of drag associated with a thick continental root (as confirmed from comparative examination of local viscous dissipation), and it encounters the uplifted phase transition much earlier. This characteristic time is slightly shorter in the case of a positive Clapeyron slope, relative to the corresponding case of a zero Clapeyron slope, because in the absence of collisional locking the Clapeyron-positive phase change directly accelerates slab sinking. The no-continent case also exhibits multiple local maxima, resulting from the absence of a continent which in turn permits the development of the full cyclicity of slab buckling (Čížková and Bina, 2013; Arredondo and Billen, 2017).

4.6. Coupled effects on stress fields of phase transitions and initial separation distance

Fig. 7 further shows that, with increasing initial separation value, the incremental stress effect of having a phase transition at 410 km depth decreases (from ∼100 MPa at 300-km initial separation to ∼50 MPa at 400-km separation, for example). This trend is related to the temporal offset between contact with the (uplifted) 410-km transition and full collision (loss of crust). In other words, it involves the mutual timing of collision and the moment when the slab tip crosses the phase transition. The reference case with

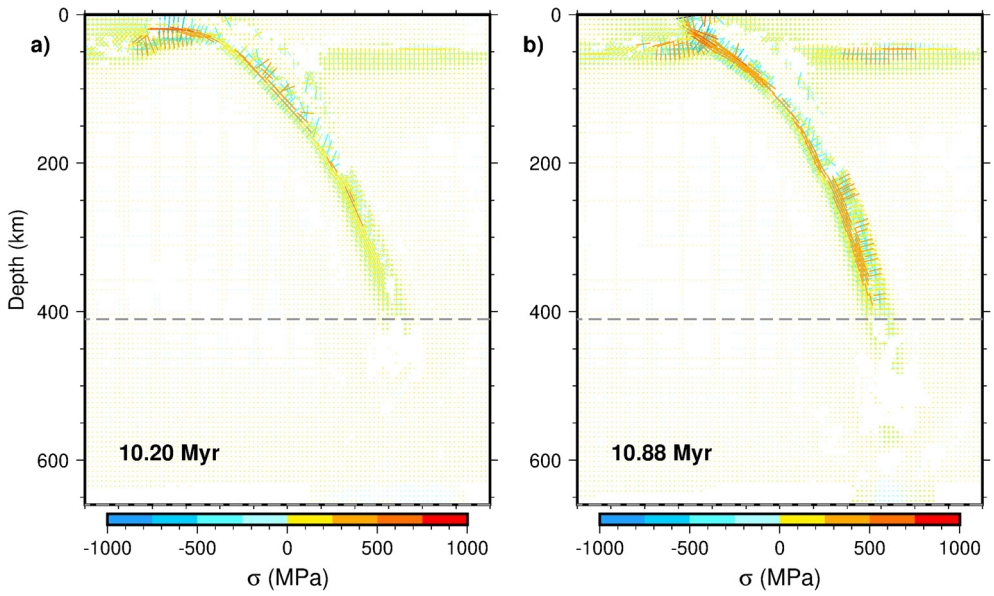

Fig. 6. Evolution of orientations and magnitudes of principal deviatoric stresses for reference case, illustrating combined effects of 410-km phase transition and ongoing collision. Warm colors (positive values) denote extension, and cold colors (negative values) denote compression. Vector lengths are proportional to stress magnitudes. Dashed line marks 410-km depth. Frames are for times 10.20 Myr (a: left) and 10.88 Myr (b: right), just before and just after slab experiences effect of (thermally uplifted) 410-km discontinuity during progress of collision. Note increase in both dip and magnitude of intermediate-depth tensional stresses between snapshots, as effect of negative petrological buoyancy arising from thermal uplift of 410-km phase transition takes hold.

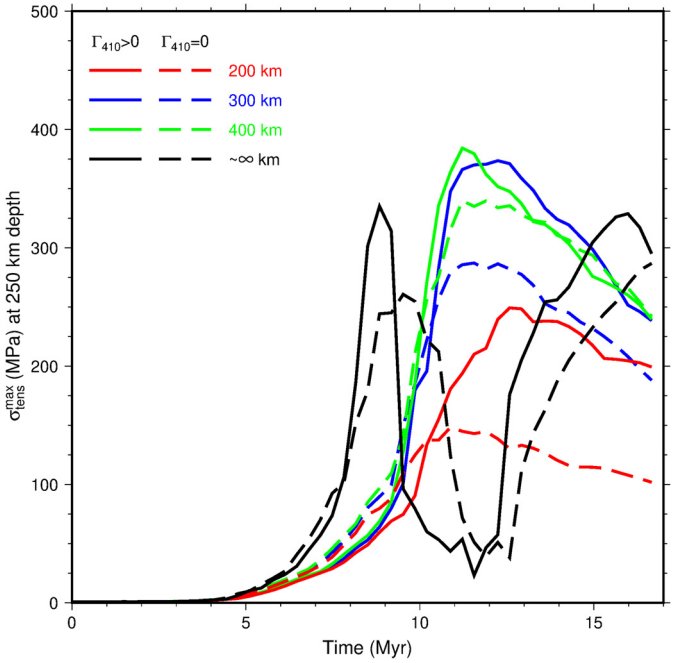

Fig. 7. Temporal evolution of magnitude of maximum deviatoric principal extensional stress at depth of 250 km in model slab during first 17 Myr (after which effects of 660-km boundary become dominant). Solid lines are for reference case with 200-km (red), 300-km (blue), and 400-km (green) initial separation. Correspondingly colored dashed lines are for cases of zero 410-km Clapeyron slope (i.e., no petrological buoyancy). Black lines are for case of no incoming continent (effectively infinite initial separation).

400-km separation collides after the tip crosses the phase transition, and thereafter the subducting plate can react to the increased pull of the slab via increased plate velocity (by up to ∼7 cm/yr). In the case with the shortest separation of 200 km, the subducting plate is already locked at the moment when the tip crosses the phase transition, and plate velocity thus cannot adjust to the increased pull; this pull therefore must be accommodated through increased stress in the hanging slab.

Moreover, if we look again (Fig. 7) at corresponding cases for zero and positive Clapeyron slopes and further assess the pattern of the increment in stress value at the local maximum discussed above, we see that the increment for the no-continent case falls in between the 400-km separation and 300-km separation values, rather than below the 400-km separation value as might perhaps have been expected. In other words, the general pattern is for the phase-transition-induced stress increment to decrease with increasing separation distance, and because the no-continent case is essentially a case of infinite separation distance, one might expect its stress increment to fall below the value for 400-km separation, but it does not. This arises because, while the increment for the 400-km case is limited by the restricted scope for post-locking rotation of the slab to a steeper dip angle, prior to resistant coupling with the lower mantle (Čížková and Bina, 2015; Goes et al., 2017), as noted above, in the no-continent case there is no locking, yet a somewhat steeper dip angle is attained earlier due to faster subduction and the strain-rate-dependent rheology of the slab. Furthermore, the no-continent case with a Clapeyron-zero phase transition exhibits shallower dip, due to the faster rollback generally observed in such Clapeyron-zero models (Čížková and Bina, 2013).

4.7. Spatial distribution of maximum shear stresses

Finally, we examine the magnitude of the maximum shear stress, as derived from the second invariant of the stress tensor, for the reference case. Fig. 8 illustrates this quantity for the reference case in snapshots for times of 10.20 Myr and 10.88 Myr (the same time frames as in Fig. 6), just before and after the slab begins to experience the effect of the (thermally uplifted) 410-km discontinuity during the progress of collision, as well as for the case in which the Clapeyron slope is set to zero (thereby eliminating petrological buoyancy). Here it is evident that the largest values of maximum shear stress in the slab occur at depths of ∼200 km or shallower. If maximum shear stress affects seismogenic potential (Islam, 2009; Joshi and Hayashi, 2010), then this may help to explain the aseismic nature of any putative deeper portions of the slab to ∼400 km depth beneath Mindoro, although this analysis

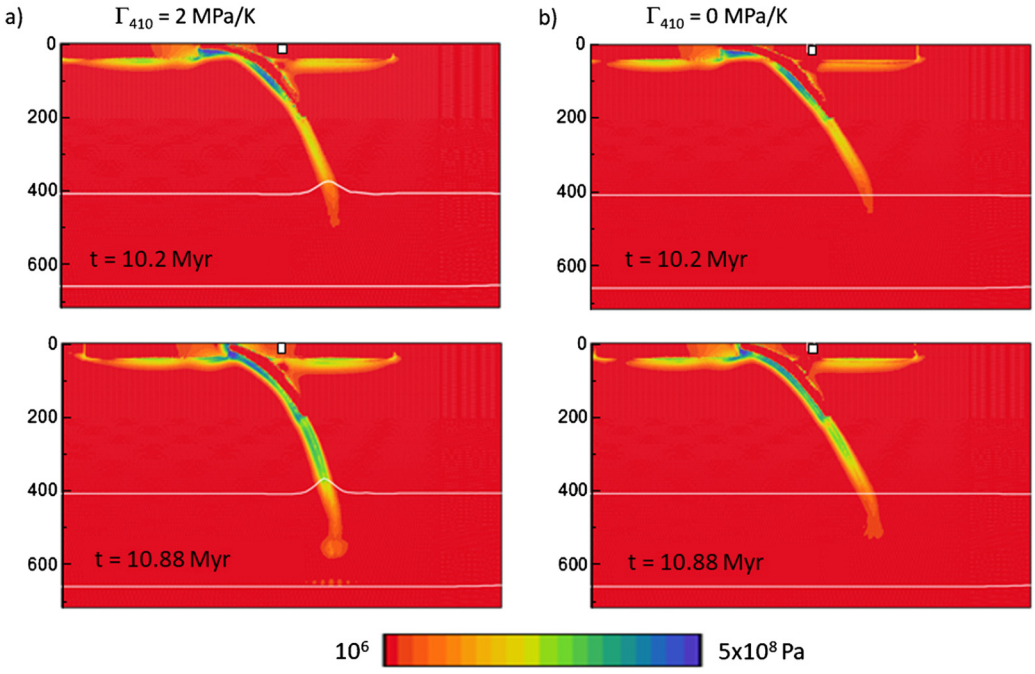

Fig. 8. Snapshots (1:1) of magnitude of maximum shear stress (as derived from second invariant of deviatoric stress) for reference case (with 400-km initial separation). Dashed line marks 410-km depth. Frames are for times 10.20 Myr and 10.88 Myr (the same time-steps as in Fig. 6). Left (a): case of normal 410-km Clapeyron slope. Right (b): case of zero 410-km Clapeyron slope. Note that largest values in slab occur at depths <200 km. If maximum shear stress affects seismogenic potential, this may explain aseismic nature of deeper portion of slab to ∼400 km beneath the Mindoro region. (Note that color scale allowing for representation of the maximum lithospheric stresses renders small crustal stresses indiscernible.)

is probably not directly applicable to aseismicity beneath central Taiwan due to the large temporal differences. Furthermore, it can be seen that interaction with the Clapeyron-positive phase transition both steepens the slab dip and significantly enhances the maximum shear stress within the slab in the ∼200-400 km depth range.

5. Discussion and conclusions

The region of the Manila Trench northwest of Mindoro Island provides a natural laboratory for studying the evolution of subduction during arc-continent collision. The variation from ongoing convergence northward along the trench to locked suturing southward permits the use of distance along the trench as an effective proxy for time in a suitable geodynamic model. This allows for comparison of trends in evolution of slab dip angles and stress fields, during progress of subduction and onset of collision, as seen in the dynamical models and in seismological observations.

Such dynamical modeling reveals the evolution of slab dip angle, beginning with initial shallowing of dip due to slab rollback (trench retreat) as the intrinsically buoyant continental material approaches the trench. Soon thereafter, slab rollback is no longer possible, due to the proximity of buoyant continental material on the incoming subducting plate, resulting in steepening of dip due to the negative thermal buoyancy of the slab. The cold thermal halo of the slab, in conjunction with the positive Clapeyron slope of the wadsleyite-forming reaction, induces upward deflection of this equilibrium “410-km” phase transition. As the tip of the slab begins to interact with the uplifted phase transition, a negative petrological buoyancy is added to the negative thermal buoyancy, further enhancing the steepening of slab dip. Relative timing of the onset of the negative petrological buoyancy contribution is affected by the initial separation distance between incoming and overriding continental fragments. As dip angle increases, the trench-slab distance naturally decreases.

Matching trends are seen in the seismological observations along the Manila Trench, as slab dip angle increases from regions of ongoing convergence in the north to fully locked collision in the south off SW Mindoro Island. Similarly, slab-trench distance (as determined from distance to the Wadati-Benioff zone of seismicity at 200 km) decreases as dip angle increases to the southeast along the arc. Such increases in dip angle are driven by the negative thermal and petrological buoyancies of the slab, where the latter accelerates the rate of increase in dip beyond the effect of solely the former (by, for example, ∼5-15° over 20 Myr).

Dynamical modeling also reveals the evolution of patterns of principal deviatoric stresses in the downgoing slab. These are dominated by down-dip tensional regimes, in which the down-dip orientation of the maximum extensional principal stress steepens along with the slab dip angle. Again, both the negative thermal buoyancy of the slab and the negative petrological buoyancy (arising from thermal uplift of the equilibrium “410-km” wadsleyite-forming phase transition as governed by its positive Clapeyron slope) result not only in increasing plunge of the maximum extensional stress direction but also in growth in the magnitude of the maximum extensional principal stress at a given fixed sampling depth, where the petrological buoyancy makes a contribution of order 100 MPa above the level contributed by thermal buoyancy alone. Furthermore, examination of the distribution of the magnitude of the maximum shear stress, as derived from the calculated principal deviatoric stresses, shows that the largest values of maximum shear stress in the slab occur at depths of ∼200 km or shallower.

Again, matching trends are seen in the seismological observations along the Manila Trench, as earthquake focal mechanisms illuminate a predominantly down-dip tensional regime, even as slab dip angles increase from north to south along the trench. Furthermore, while recorded seismicity is generally limited to depths shallower than 250 km, tomographic imaging suggests aseismic extension of the slab to ∼400 km depth, consistent with a sce-

nario in which seismogenic potential is affected by the magnitude of maximum shear stress.

Concomitant changes in dip angles and stress fields due to coupled effects of phase transitions and initial continental separation distances are also evident in the models. In general, dip angles grow steeper due to phase transition more rapidly in cases of smaller initial separation, and extensional stress increments due to phase transition are larger in cases of smaller initial separation. This happens because the leading tips of longer slabs arising from larger separation distances encounter the negative-buoyancy-enhancing, thermally uplifted phase transition while they are still in convergence mode, with abundant oceanic crust remaining to lubricate subduction, so that they can respond to the increased slab-pull force via increased plate velocity. The tips of shorter slabs arising from smaller separation distances, on the other hand, encounter the phase transition when they are already in collision mode, with all oceanic crust already having been consumed, and because they thus cannot respond to the increased pull through change in plate velocity, they accommodate it through rotation of the slab toward the vertical along with increased extensional stress in the hanging slab.

Overall, the good model correspondence with seismological observations of the evolution of dip and stress in this region is achieved by our reference case, in which initial continental separation of 400 km allows the slab tip to encounter the thermally uplifted 410-km phase transition prior to total loss of oceanic crust upon full collision. The model with 300-km initial separation may be considered a slightly better fit, however, in that dip angles are seen to increase toward 90° more rapidly (and stresses acquire a larger contribution from the petrological buoyancy force), as the earlier loss of crust in this case limits its ability to respond through increased plate velocity, thereby driving greater slab rotation and extension. Both of these models forecast eventual detachment of the nearly vertically hanging slab.

Model dip angles may, of course, be affected to some extent by initial conditions of dip and crustal strength (Tagawa et al., 2007a, 2007b). Exploratory testing indicates that the initial arc curvature of the subducting plate can affect dip magnitude, but the time evolution of the dip angle remains the same, essentially yielding dip–vs.–time curves with fixed offset throughout the evolution. Similarly, lower initial crustal viscosity can slightly increase the dip angle but again as a fixed offset, yielding temporal variations of identical character. Here, however, we are interested primarily in observing trends in dip-angle evolution, rather than in reproducing specific values. Variations in continental crustal density may also slightly affect dip angles. A continental fragment tends to stop subduction by two mechanisms – it is more buoyant and at the same time more viscous so that the lubricating effect is significantly reduced – both of which inhibit subduction so that the plate rotates towards the vertical. Density variations thus may affect the absolute value of the dip angle but again not the overall trend that we are seeking.

The region of the Manila Trench in general, and of Mindoro Island in particular, consists of highly complex three-dimensional structures (Fan et al., 2015, 2016, 2017), perhaps comparable to those encountered in the eastern Mediterranean (Menant et al., 2016), which we have made no effort to attempt to reproduce here. Indeed, it is remarkable that such a simple two-dimensional geodynamical model can reasonably reproduce such features of evolving dip angles and stress patterns as are observed in seismotectonic studies of the area, by our simple expedient of mapping distance along the arc – which corresponds tectonically to degree of arc-continent subduction closure or collision – into a proxy for time. It has been noted, however, that the generally observed horizontality of the intermediate principal stress axis in many subduction-related seismic focal mechanisms suggests a significant 2D component (in a subvertical plane) to such seismic stress fields in general, thereby supporting the frequently reasonable applicability of 2D geodynamic modeling even in such complex 3D scenarios (Helffrich, 2018).

Acknowledgements

The authors are grateful to Jianke Fan for generously providing a preprint of Fan et al. (2017) prior to publication. This work was supported by the W.V. Jones II endowment at Northwestern University (CB), the Czech Science Foundation under project number 18-20818S (HČ), and the Taiwan Earthquake Research Center (TEC) through Ministry of Science and Technology (MOST) grant number 107-2117-M-008-010. The TEC contribution number for this article is 00157. Several figures were produced using the Generic Mapping Tool (GMT) software (Wessel and Smith, 1998). CB is grateful to the Department of Geophysics at Charles University in Prague, the Department of Earth Sciences at National Central University in Taiwan, and the Geodynamics Research Center at Ehime University in Matsuyama, Japan, for generous support of visits during the course of this work. The authors thank two anonymous reviewers for their detailed comments on the manuscript.

Appendix

Rheology:

The composite rheological model (van den Berg et al., 1993) combines diffusion creep, dislocation creep, and a power-law stress-limiter (van Hunen et al., 2002). The effective viscosity is obtained from the viscosities of individual creep mechanisms:

$$\eta_{\mathrm{eff}} = \left(\frac{1}{\eta_{\mathrm{diff}}} + \frac{1}{\eta_{\mathrm{disl}}} + \frac{1}{\eta_y} \right)^{-1}$$

Here η_{diff}, η_{disl}, and η_y are viscosities of diffusion creep, dislocation creep, and stress-limiter respectively:

$$\eta_{\mathrm{diff}} = \frac{1}{A_{\mathrm{diff}}} \exp\left(\frac{E_{\mathrm{diff}} + \mathrm{pV}_{\mathrm{diff}}}{\mathrm{RT}} \right)$$

$$\eta_{\mathrm{disl}} = \frac{1}{A_{\mathrm{disl}}^{\frac{1}{n}}} e^{(1-n)/n} \exp\left(\frac{E_{\mathrm{disl}} + \mathrm{pV}_{\mathrm{disl}}}{\mathrm{nRT}} \right)$$

$$\eta_y = \tau_y e_y^{-1/n_y} e^{1/n_y - 1}$$

Upper mantle activation parameters are based on Hirth and Kohlstedt (2003). In the lower mantle we assume only diffusion creep, with activation parameters based on slab sinking speed analysis (Čížková et al., 2012). For meanings of symbols and parameter values, see Table 1.

Thermal expansivity:

Thermal expansivity decreases with depth (Chopelas and Boehler, 1992; Katsura et al., 2009) and is reduced by a factor of ~3 across the whole mantle depth extent. Here we parameterize its depth dependence by the formula used by Hansen and Yuen (1994):

$$\alpha = \alpha_0 \frac{\Delta\alpha}{[(\Delta\alpha^{1/3} - 1)(1 - z) + 1]^3}$$

Surface value α_0 and contrast over the mantle $\Delta\alpha$ are given in Table 1; z is dimensionless depth.

References

Arredondo, K.M., Billen, M.I., 2016. The effects of phase transitions and compositional layering in two-dimensional kinematic models of subduction. J. Geodyn. 100, 159–174. https://doi.org/10.1016/j.jog.2016.05.009.

Arredondo, K.M., Billen, M.I., 2017. Coupled effects of phase transitions and rheology in 2D dynamical models of subduction. J. Geophys. Res., Solid Earth 122, 5813–5830. https://doi.org/10.1002/2017JB014374.

Baumann, C., Gerya, T.V., Connolly, J.A.D., 2010. Numerical modelling of spontaneous slab breakoff dynamics during continental collision. In: Advances in Interpretation of Geological Processes: Refinement of Multi-scale Data and Integration in Numerical Modelling. In: Geological Society, London, Special Publications, vol. 332, pp. 99–114.

Běhounková, M., Čížková, H., 2008. Long-wavelength character of subducted slabs in the lower mantle. Earth Planet. Sci. Lett. 275, 43–53.

Bina, C.R., 1997. Patterns of deep seismicity reflect buoyancy stresses due to phase transitions. Geophys. Res. Lett. 24, 3301–3304. https://doi.org/10.1029/97gl53189.

Bina, C.R., Helffrich, G., 1994. Phase transition Clapeyron slopes and transition zone seismic discontinuity topography. J. Geophys. Res. 99 (B8), 15853–15860.

Chen, P.-F., Bina, C.R., Okal, E.A., 2001. Variations in slab dip along the subducting Nazca Plate, as related to stress patterns and moment release of intermediate-depth seismicity and to surface volcanism. Geochem. Geophys. Geosyst. 2. https://doi.org/10.1029/2001GC000153.

Chen, P.-F., Bina, C.R., Okal, E.A., 2004a. A global survey of stress orientations in subducting slabs as revealed by intermediate-depth earthquakes. Geophys. J. Int. 159, 721–733. https://doi.org/10.1111/j.1365-246X.2004.02450.x. Erratum, 2005. Geophys. J. Int. 161, 419. https://doi.org/10.1111/j.1365-246X.2005.02548.x.

Chen, P.-F., Huang, B.-S., Liang, W.-T., 2004b. Evidence of a slab of subducted lithosphere beneath central Taiwan from seismic waveforms and travel times. Earth Planet. Sci. Lett. 229, 61–71.

Chen, P.-F., Olavere, E.A., Lee, K.-M., Bautista, B.C., Solidum Jr., R.U., Huang, B.-S., 2018. Upper mantle velocity structures beneath northwest Mindoro as revealed by teleseismic relative arrival times. Unpublished data.

Chen, P.-F., Olavere, E.A., Wang, C.-W., Bautista, B.C., Solidum Jr., R.U., Liang, W.-T., 2015. Seismotectonics of Mindoro, Philippines. Tectonophysics 640–641, 70–79. https://doi.org/10.1016/j.tecto.2014.11.023.

Chopelas, A., Boehler, R., 1992. Thermal expansivity in the lower mantle. Geophys. Res. Lett. 19, 1983–1986.

Čížková, H., Bina, C.R., 2013. Effects of mantle and subduction-interface rheologies on slab stagnation and trench rollback. Earth Planet. Sci. Lett. 379, 95–103. https://doi.org/10.1016/j.epsl.2013.08.011.

Čížková, H., Bina, C.R., 2015. Geodynamics of trench advance in a Philippine-Sea-style geometry. Earth Planet. Sci. Lett. 430, 408–415. https://doi.org/10.1016/j.epsl.2015.07.004.

Čížková, H., Bina, C.R., 2019. Linked influences on slab stagnation: interplay between lower mantle viscosity structure, phase transitions, and plate coupling. Earth Planet. Sci. Lett. 509, 88–99. https://doi.org/10.1016/j.epsl.2018.12.027.

Čížková, H., van den Berg, A.P., Spakman, W., Matyska, C., 2012. The viscosity of Earth's lower mantle inferred from sinking speed of subducted lithosphere. Phys. Earth Planet. Inter. 200–201, 56–62.

Čížková, H., van Hunen, J., van den Berg, A.P., 2007. Stress distribution within subducting slabs and their deformation in the transition zone. Phys. Earth Planet. Inter. 161, 202–214.

Duretz, T., Gerya, T.V., May, D.A., 2011. Numerical modelling of spontaneous slab breakoff and subsequent topographic response. Tectonophysics 502, 244–256.

Ekström, G., Nettles, M., Dziewonski, A.M., 2012. The global CMT project 2004-2010: centroid-moment tensors for 13,017 earthquakes. Phys. Earth Planet. Inter. 200–201, 1–9. https://doi.org/10.1016/j.pepi.2012.04.002.

Engdahl, E.R., van der Hilst, R., Buland, R., 1998. Global teleseismic earthquake relocation with improved travel times and procedures for depth determination. Bull. Seismol. Soc. Am. 88, 722–743.

Fan, J., Wu, S., Spence, G., 2015. Tomographic evidence for a slab tear induced by fossil ridge subduction at Manila Trench, South China Sea. Int. Geol. Rev. 57 (5–8), 998–1013. https://doi.org/10.1080/00206814.2014.929054.

Fan, J., Zhao, D., Dong, D., 2016. Subduction of a buoyant plateau at the Manila Trench: tomographic evidence and geodynamic implications. Geochem. Geophys. Geosyst. 17, 571–586. https://doi.org/10.1002/2015GC006201.

Fan, J., Zhao, D., Dong, D., Zhang, G., 2017. P-wave tomography of subduction zones around the central Philippines and its geodynamic implications. J. Asian Earth Sci. 146, 76–89. https://doi.org/10.1016/j.jseaes.2017.05.015.

François, T., Burov, E., Agard, P., Meyer, B., 2014. Buildup of a dynamically supported orogenic plateau: numerical modeling of the Zagros/Central Iran case study. Geochem. Geophys. Geosyst. 15, 2632–2654. https://doi.org/10.1002/2013GC005223.

Ghazian, R.K., Buiter, S.J.H., 2013. A numerical investigation of continental collision styles. Geophys. J. Int. 193, 1133–1152. https://doi.org/10.1093/gji/ggt068.

Goes, S., Agrusta, R., van Hunen, J., Garel, F., 2017. Subduction-transition zone interactions: a review. Geosphere 13, 644–664. https://doi.org/10.1130/GES01476.1.

Hamburger, M.W., Galgana, G.A., Bacolcol, T., McCaffrey, R., Yu, S., 2010. Analysis of oblique plate convergence along the Manila Trench and the Philippine Trench. In: AGU Fall Meeting Abstracts. T51D-2084.

Hansen, U., Yuen, D.A., 1994. Effects of depth-dependent thermal expansivity on the interaction of thermal-chemical plumes with a compositional boundary. Phys. Earth Planet. Inter. 86, 205–221.

Helffrich, G., 2018. Comments, Discussion Session 2. In: 2nd Asia-Pacific Workshop on Lithosphere and Mantle Dynamics. Yokohama, Japan, August 5, 2018.

Hirth, G., Kohlstedt, D., 2003. Rheology of the upper mantle and mantle wedge: a view from the experimentalists. In: Inside the Subduction Factory. In: Geophys. Monogr., vol. 138. American Geophysical Union, Washington, DC.

Islam, M., 2009. Cohesive strength and seismogenic stress pattern along the active basement faults of the Precordillera-Sierras Pampeanas ranges, western Argentina: an experimental analysis by means of numerical model. J. Mt. Sci. 6, 331–345. https://doi.org/10.1007/s11629-009-1013-7.

Ito, E., Sato, H., 1992. Effect of phase transformations on the dynamics of the descending slab. In: Syono, Y., Manghnani, M.H. (Eds.), High-Pressure Research: Application to Earth and Planetary Sciences. AGU, Washington, D.C., pp. 257–262.

Joshi, G.R., Hayashi, D., 2010. Numerical modeling of seismogenic stress pattern and cohesive strength along the Main Himalayan décollement thrust zone, NW-Himalaya. Geophys. Res. Abstr. 12, EGU2010-7684-2.

Katsura, T., Yokoshi, S., Kawabe, K., Shatskiy, A., Manthilake, M.A.G.M., Zhai, S., Fukui, H., Hegoda, H.A.C.I., Yoshino, T., Yamazaki, D., Matsuzaki, T., Yoneda, A., Ito, E., Sugita, M., Tomioka, N., Hagiya, K., Nozawa, A., Funakoshi, K., 2009. P–V–T relations of $MgSiO_3$ perovskite determined by in situ X-ray diffraction using a large-volume high-pressure apparatus. Geophys. Res. Lett. 36, L01305.

Magni, V., van Hunen, J., Funiciello, F., Faccenna, C., 2012. Numerical models of slab migration in continental collision zones. Solid Earth 3, 293–306. https://doi.org/10.5194/se-3-293-2012.

Mason, W.G., Moresi, L., Betts, P.G., Miller, M.S., 2010. Three-dimensional numerical models of the influence of a buoyant oceanic plateau on subduction zones. Tectonophysics 483, 71–79.

Menant, A., Sternai, P., Jolivet, L., Guillou-Frottier, L., Gerya, T., 2016. 3D numerical modeling of mantle flow, crustal dynamics and magma genesis associated with slab roll-back and tearing: the eastern Mediterranean case. Earth Planet. Sci. Lett. 442, 93–107. https://doi.org/10.1016/j.epsl.2016.03.002.

Sarewitz, D.R., Karig, D.E., 1986. Geologic evolution of Western Mindoro Island and the Mindoro Suture Zone, Philippines. J. Southeast Asian Earth Sci. 1, 117–141. https://doi.org/10.1016/0743-9547(86)90026-7.

Segal, A., Praagman, N., 2005. The SEPRAN FEM Package. Technical report. Delft Univ. Technol., Ingenieursbureau SEPRA, The Netherlands. http://ta.twi.tudelft.nl/sepran/sepran.html.

Steinbach, V., Yuen, D.A., 1995. The effects of temperature dependent viscosity on mantle convection with two mantle major phase transitions. Phys. Earth Planet. Inter. 90, 13–36.

Tagawa, M., Nakakuki, T., Kameyama, M., Tajima, F., 2007a. The role of history-dependent rheology in plate boundary lubrication for generating one-sided subduction. Pure Appl. Geophys. 164, 879–907. https://doi.org/10.1007/s00024-007-0197-4.

Tagawa, M., Nakakuki, T., Tajima, F., 2007b. Dynamical modeling of trench retreat driven by the slab interaction with the mantle transition zone. Earth Planets Space 59, 65–74.

Teng, L.S., 1990. Geotectonic evolution of Late Cenozoic arc-continent collision in Taiwan. Tectonophysics 183, 57–76.

van den Berg, A.P., van Keken, P.E., Yuen, D.A., 1993. The effects of a composite non-Newtonian and Newtonian rheology on mantle convection. Geophys. J. Int. 115, 62–78.

van Hunen, J., van den Berg, A.P., Vlaar, N.J., 2002. On the role of subducting oceanic plateaus in the development of shallow flat subduction. Tectonophysics 352, 317–333.

Wessel, P., Smith, W.H.F., 1998. New, improved version of the Generic Mapping Tools Released. Eos, Trans. Am. Geophys. Union 79, 579.

Yumul Jr., G.P., Dimalanta, C.B., Tamayo, R.A., Maury, R.C., 2003. Collision, subduction and accretion events in the Philippines: a synthesis. Isl. Arc 12 (2), 77–91.

Zahirovic, S., Seton, M., Müller, R.D., 2014. The Cretaceous and Cenozoic tectonic evolution of Southeast Asia. Solid Earth 5, 227–273. https://doi.org/10.5194/se-5-227-2014.

Zahradník, J., Čížková, H., Bina, C.R., Sokos, E., Janský, J., Tavera, H., Carvalho, J., 2017. A recent deep earthquake doublet in light of long-term evolution of Nazca subduction. Sci. Rep. 7, 45153. https://doi.org/10.1038/srep45153.